J. Fluid Mech. (1996), vol. 318, pp. 273–302

Experimental evidence of the rapid distortion of turbulence in the air flow over water waves

By C. MASTENBROEK[1]†, V. K. MAKIN[1], M. H. GARAT[2] AND J. P. GIOVANANGELI[2]

[1] Royal Netherlands Meteorological Institute (KNMI), PO Box 201, 3730 AE De Bilt, The Netherlands

[2] Institut de Recherche sur les Phénomènes Hors Equilibre Laboratoire I.O.A., Parc Scientifique et Technologique de Luminy. Case 903, 163 Avenue de Luminy, 13288 Marseille Cedex 9, France

(Received 11 February 1995 and in revised form 19 February 1996)

Detailed observations of the air flow velocity, pressure and Reynolds stresses above water waves in a wave flume are presented. The static pressure fluctuations induced by the waves are observed following a new procedure that eliminates acoustical contamination by the wave maker. The measurements are analysed by comparing them with numerical simulations of the air flow over waves. In these numerical simulations the sensitivity to the choice of turbulence closure is studied. We considered both first-order turbulence closure schemes based on the eddy viscosity concept, and a second-order Reynolds stress model. The comparison shows that turbulence closure schemes based on the eddy viscosity concept overestimate the modulation of the Reynolds stress in a significant part of the vertical domain. When an eddy viscosity closure is used, the overestimated modulation of the Reynolds stress gives a significant contribution to the wave growth rate. Our results confirm the conclusions Belcher & Hunt reached on the basis of the rapid distortion theory.

The ratio of the wind speed to the phase speed of the paddle wave in the experiment varies between 3 and 6. The observed amplitudes of the velocity and pressure perturbation are in excellent agreement with the simulations. Comparison of the observed phases of the pressure and velocity perturbations shows that the numerical model underpredicts the downwind phase shift of the undulating flow.

The sheltering coefficients for the flow over hills and the growth rates of waves that are slow compared to the wind calculated with the Reynolds stress model are in excellent agreement with the analytical model of Belcher & Hunt. Extending the calculations to fast waves, we find that the energy flux to waves travelling almost as fast as the wind is increased on going from the mixing length turbulence closure to the Reynolds stress model.

1. Introduction

Though the subject has been studied for decades, the mechanisms responsible for the growth of ocean waves by wind are still not well understood. Both observations in the field (Snyder *et al.* 1981) and in the laboratory (compiled by Plant 1982) tend to show larger growth rates than can be understood with the present models. To describe the interaction between the wave-induced motions in the air flow and the

---

† Present address: ARGOSS, PO Box 61, 8325 ZH Vollenhove, The Netherlands.

turbulence, models of increasing complexity have been used. In the classical theory of Miles (1957) this interaction is neglected completely, and turbulence serves only to maintain a logarithmic wind profile. Jacobs (1987) and van Duin & Janssen (1992) use a mixing length type approach to calculate the modulations of the Reynolds stress caused by wave-induced motions. The earliest numerical simulations of the air flow over waves, e.g. Gent & Taylor (1976) and Chalikov (1978), used a one-equation e-model. Later Al-Zanaidi & Hui (1984) used a more general two-equation closure scheme. However, they all took the eddy viscosity concept as their starting point.

For the related problem of wind over hills, Britter, Hunt & Richards (1981) suggested that this concept can only be valid in a thin layer adjacent to the surface, which was termed the *inner region*. Outside this layer, in the *outer region*, the turbulence is distorted too rapidly for the eddy viscosity concept to be valid, and the rapid distortion theory as described by Batchelor & Proudman (1954) should be applied. In his numerical calculations Townsend (1972) took into account the finite relaxation time of the turbulent eddies. Later this model was refined by Townsend (1980) to account for the effects of the rapid distortion mechanism. Hunt, Leibovich & Richards (1988) developed a four-layer asymptotic model to describe the changes to the air flow passing over hill. Recently this model was extended by Belcher & Hunt (1993) to the case of shear flow over slowly moving waves.

The aim of this paper is to present and analyse detailed observations of the air flow velocity, pressure fluctuations and turbulent moments over mechanically generated water waves in a wind wave tank. For this a sophisticated experimental set-up has been used. Horizontal and vertical air flow velocity components were determined by means of a X-wire anemometer. Fluctuations of the static pressure were monitored by means of an new type of pressure probe. Pressure measurements in a wind-wave tank can get easily contaminated with noise made by the wave maker. This contamination was avoided by switching off the wave maker before the data acquisition was started.

The observations are compared with results of numerical simulations using three different closure hypotheses: a mixing length closure, a two-equation e-ϵ model and a second-order Reynolds stress model. The motivation of this study is that very few comparisons between models with different turbulence schemes and detailed observations of the air flow over water waves have been made. Observations of stress profiles over hills have shown that models based on the eddy viscosity hypothesis overestimate the shear stress modulation outside the inner region (Belcher, Newley & Hunt 1993). This study aims to show that the same is true for flow over water waves.

Similar experiments done in the past differ in several respects from the experiment described here. The first to make detailed observations of the air flow over waves was Stewart (1970). As he used relatively short paddle waves (0.41 m) in combination with low wind speeds, the wave Reynolds number in his experiment was an order of magnitude smaller than is the case in the present experiment. On the basis of the model calculations presented by Harris, Belcher & Street (1996) it is to be expected that the low Reynolds number will complicate the analysis of the Stewart experiment. Later, experiments involving a wave follower were done by Hsu, Hsu & Street (1981) and Hsu & Hsu (1983) in the Stanford wind tunnel. A good analysis of these experiments can be found in Harris *et al.* (1996). The Stanford experiments differ in several respects from the experiment presented here. The fetch in the IRPHE wind tunnel used in the present experiments is 28 m, twice the fetch in the Stanford experiment. Due to the relatively short fetch in the Stanford tank, Harris *et al.* (1996) suspected that the turbulence in the outer region was not fully developed. Since this is the region where the largest difference between the turbulence schemes can be expected, no strong conclusions regarding the validity of these schemes can be based on these experiments. The ratio of the wind speed to the phase speed in the Stanford experiments ranged from less than 1 to 2. The failure of the eddy viscosity models is expected to be most apparent above waves slow compared to the wind. By using both a shorter paddle wave (0.8 m compared to 1.6 m) and larger wind speeds we were able to increase the wind speed/phase speed ratio to a value of 6. Another difference is that in the Stanford experiments the probes were mounted on a wave-follower, which made it possible to make observations close to the surface. The experiments in the Stanford wind tunnel and the present experiment can be considered complementary: owing to the employment of the wave follower the first experiment gives a good picture of the dynamics in the (upper part of the) inner region; owing to the longer fetch the present experiment is better suited to study the outer region.

2. Measurements

2.1. *The experimental set-up in the IRPHE wave tank*

The experiments were conducted in the large IRPHE Wind Wave Tank† described in detail by Favre & Coantic (1974). It consists mainly of a water tank which is 40 m long, 3 m wide and 1 m deep. Above the water surface a closed loop wind tunnel produces an air flow, with wind speeds of up to 16 m s^{-1}. The height of the air column is close to 2 m. The experiments are done at a fetch of 28 m. At this fetch the wind profile is observed to be logarithmic up to 40 cm above the water surface.

The experiment consisted of three runs. During each run the mean value of the wind velocity in the potential flow above the turbulent boundary layer was kept constant at 6.3, 5.4 and 3.5 m s^{-1}, respectively. The paddle waves were generated by means of a wave maker at the entrance of the water tank. The wave maker was completely submerged, in order not to disturb the air flow.

The probes were located at a fetch of 28 m. A mechanical device was used to put the probes at various heights above the mean surface. The longitudinal and the vertical turbulent velocity fluctuations were measured by means of a X-wire, with both wires mounted at a 45° angle relative to the mean wind direction. They were connected to two DISA model 55 constant-temperature anemometers. The hot wires were calibrated before and after the experiments in a small wind tunnel for mean velocities ranging from 3 up to 18 m s^{-1}. This large range is necessary because of the large fluctuations in wind speed in the turbulent air flow, particularly close to the surface. During the calibration a least-square regression law was used to relate the output voltages E_1 and E_2 of the anemometers to the effective cooling velocities U_{eff_1} and U_{eff_2}, using the Collis and Williams cooling law:

$$E_i^2 = A_i + B_i * U_{eff_i}^{n_i}, \tag{2.1}$$

where $i = 1, 2$ denotes the wires. The effective velocities U_{eff_i} are related to the wind speed U by

$$U_{eff_i} = U \left(\cos^2 \Phi_i + K_i^2 \sin^2 \Phi_i\right)^{1/2}. \tag{2.2}$$

Here K_i is the cooling factor of wire i, and Φ_i is the angle between the wind vector and the normal to wire i. Since the wires are mounted perpendicular to each other $\Phi_1 + \Phi_2 = \pi/2$. The coefficient A_i, B_i and n_i are determined during the calibration

---

† Formerly known as the Wind Wave Tank of the Institut de Mécanique Statistique de la Turbulence (IMST).

(Resch 1973; Giovanangeli 1980). The systematic error in the velocity observations with the X-wires is estimated to be less than 5×10^{-3} m s^{-1}.

The water surface elevations were measured using two capacitance wave gauges of 0.3 mm outer diameter with two DISA model capacitance measuring units. The typical sensitivity of the wave gauges was determined by raising and lowering the probes by known amounts. The two wave gauges were located at the same fetch of 28 m, separated from each other by 2 cm in the mean wind direction, to make direct observations of the wave slope.

The pressure fluctuations were measured using a new method (Giovanangeli 1988), whereby the static pressure is determined from the difference of the observed total pressure and the dynamical pressure derived from velocity measurements. The velocity measurements were done with the X-wires described above. The total pressure was measured using a bleed-type pressure sensor TSI model 1412 J. In this sensor a flow of helium gas through a capillary tube is created by connecting one side of the tube to a reservoir of helium at constant pressure. The other side of the tube is located inside a total pressure sensing head. The flow rate in the capillary tube depends on the pressure difference between the total pressure in the sensing head and the constant pressure in the reservoir. The flow rate is measured with a hot film sensor located near the exit of the capillary tube. The transfer function (gain and phase shift) of the pressure probe has been determined in detail in previous studies (e.g. Giovanangeli & Chambaud, 1987). It was shown that the pressure probe in combination with the method used here allows measurements of the static pressure fluctuations in air flow, particularly close to the waves, with an accuracy of 0.05 Pa.

All the output voltages given by the different probes were amplified and conditioned before being stored in a digitized form on a COMPAQ 386 at 150 Hz sampling frequency. Low-pass analog linear filters were used prior to digitization.

The key point of the experiments was to measure the static pressure fluctuations in the presence of paddle waves. Other investigators have shown that the driving mechanism can induce acoustic pressure fluctuations inside the wave tank (Latif 1974; Papadimitrakis, Hsu & Street 1986; Banner 1990). They used different methods to correct for these effects on the pressure fluctuations estimates. Our first experiments have indeed shown that when the wave maker is running it induces a strong contamination of the measurements of the amplitude of the static pressure fluctuation. Rather than trying to correct for the contamination, we chose to avoid the effect completely by turning off the wave maker before the data acquisition starts. Therefore we used the following procedure in the experiments presented here. First a continuous wave field is generated with the wave maker in the presence of wind. Then the wave paddle is suddenly stopped and the data acquisition is started. For about 30 s, corresponding to the time required for the end of the wave field to reach the experimental section, the pressure above the paddle wave can be observed without any acoustic contamination. In figure 1 spectra are shown of the elevation, pressure and vertical velocity variance, both with the paddle working and while it was switched off during the data acquisition. It is obvious that the paddle wave fields generated in the first case and in the second one are similar. From the pressure spectrum it is also clear that the noise of the wave maker working induces a large error in the measurements of the pressure, particularly at the frequency of the paddle motions. The experimental procedure we used in these experiments allows observation of the pressure fluctuations above paddle waves while avoiding completely the errors induced by the paddle motions. In figure 1 the spectra of the vertical velocity variances are also shown. These spectra show that the air flow over the waves is not affected by switching off the paddle. To

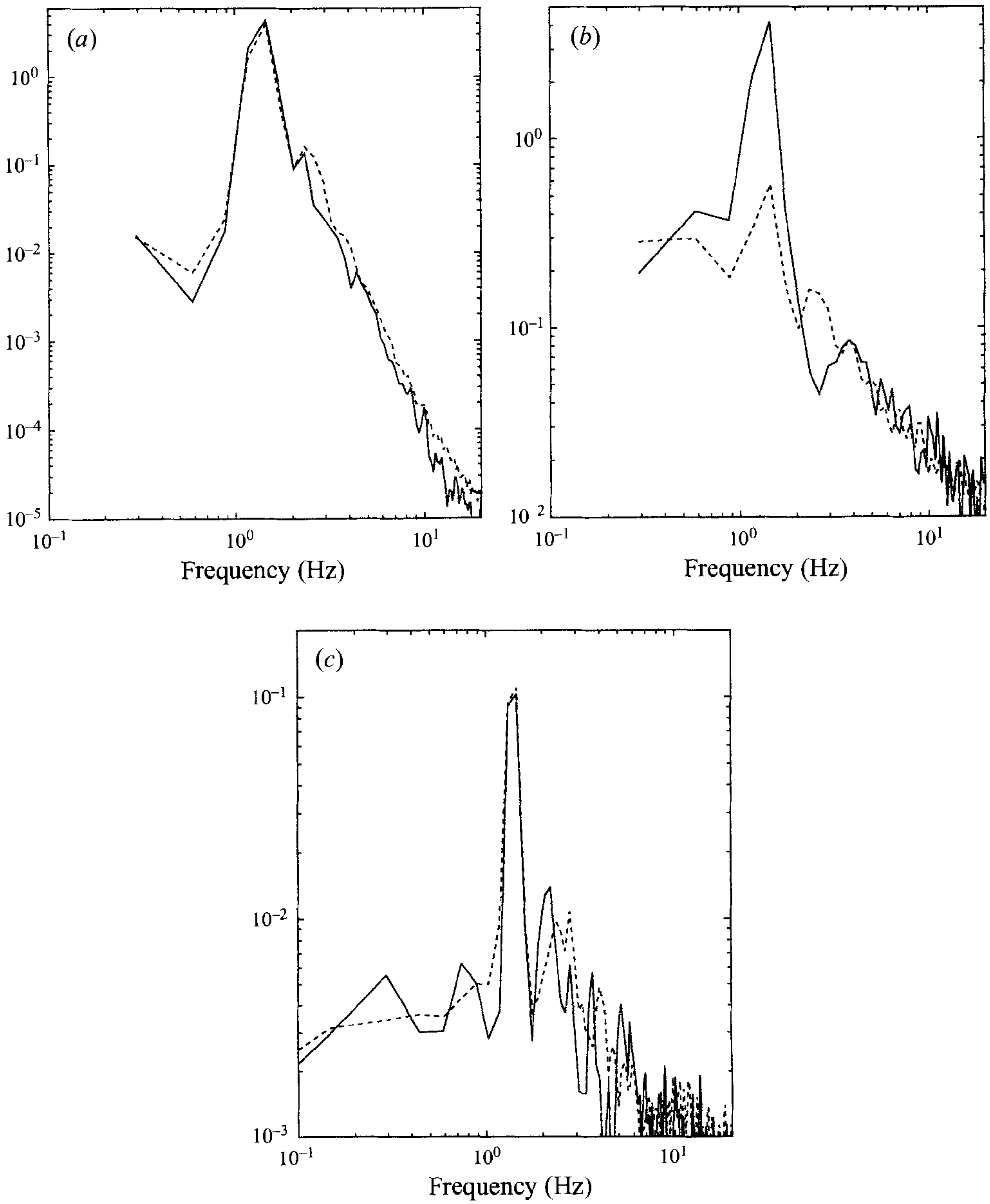

FIGURE 1. Spectra of (*a*) the elevation, (*b*) pressure and (*c*) vertical velocity variance for the case when the paddle is still working (solid line) and for when it is switched of (dashed line) during the data acquisition. The pressure and velocity measurements were done at a height of 5 cm above the mean water level, with a 5 m s^{-1} wind speed in the middle of the tunnel. The paddle waves had a length of 80 cm, and an average amplitude of 2 cm.

get times series long enough to obtain good estimates of pressure and wave spectra the procedure used here was repeated ten times.

An estimate of the phase speed $c(\omega)$ of the paddle waves was made from the phase shift $\omega\Delta t$ between the two wave gauges: $c = \Delta x/\Delta t$. The wave gauges were located $\Delta x = 2$ cm apart. It was found that the paddle wave can be considered as a free propagating deep-water gravity wave, since the observed phase speed was very close to g/ω, where g is the gravitational acceleration.

2.2. *Averaging and decomposition*

Let $q_i, i = 1,..,N$, represent one series of observations of a certain quantity at a given height. In the present experiment, this quantity can be a velocity component or the pressure. As described above, after every 30 s of observations the data acquisition is stopped and the wave maker is started to generate new paddle waves. After switching off the wave maker the data acquisition is continued. For every series this procedure was repeated ten times. With a sampling rate of 150 Hz it follows that one series consists of 45000 individual observations. Simultaneously with the velocity and pressure, the water elevation η was measured. The upward zero crossings in η_i are used to mark the border between two consecutive waves. Each individual wave is then divided into N_b bins. After sampling all data in these bins, we get a set $q_{jk}, j = 1,..,N_b, k = 1,..,N_j$, where N_j is the number of observations that fall into bin j. Following Hsu *et al.* (1981) we now define two averaging procedures. The *phase* or *ensemble* average of property q is given by

$$\bar{q}_j = \frac{1}{N_j} \sum_{k=1}^{N_j} q_{jk}. \tag{2.3}$$

The average over a wave period, or simply the *mean*, is given by

$$\langle \bar{q} \rangle = \frac{1}{N_b} \sum_{j=1}^{N_b} \bar{q}_j. \tag{2.4}$$

The deviations of an individual observation from its phase average is called the *fluctuating* part: $q'_{jk} = q_{jk} - \bar{q}_j$. As these fluctuations are mainly caused by turbulence (Hsu *et al.*, 1981), the phase average (2.3) can be regarded as an ensemble average. Therefore we will use the same symbol for the phase averaging procedure defined above and the Reynolds average. The *wave-induced* part of quantity q is defined as the deviation of the phase average from the mean: $\tilde{q}_j = \bar{q}_j - \langle \bar{q} \rangle$. Three Reynolds stress components can be found from the observations by applying the phase average (2.3) to the products $(u'u')_{jk}$, $(u'w')_{jk}$ and $(w'w')_{jk}$. In this paper we will refer to $\overline{u'u'}$ and $\overline{w'w'}$ as the horizontal and vertical velocity variance, respectively. The cross-correlation is used to define the (turbulent) stress: $\tau = -\rho_a \overline{u'w'}$.

To simplify the analysis we will often look at the amplitude of the first harmonic of the wave-induced part. Therefore we define the complex amplitude $\hat{q}$ such that

$$\tilde{q}_j = \tfrac{1}{2} \left[\hat{q} e^{i(2\pi j/N_b + \phi_\eta)} + \text{c.c.} \right] + \text{harmonics}. \tag{2.5}$$

The phase ϕ_η is chosen in such a way that the amplitude of the elevation $\hat{\eta}$ is real. This greatly simplifies the interpretation of the other (complex) amplitudes: the real part $\mathrm{Re}[\hat{q}]$ gives the amplitude of $\tilde{q}$ in phase with the elevation, and the imaginary part $\mathrm{Im}[\hat{q}]$ the amplitude 90° degrees out-of-phase with the elevation. A positive value of $\mathrm{Im}[\hat{q}]$ corresponds to an enhancement of q above the windward slope of the wave.

There are two possible sources of errors in the averaged observations. The first is due to random errors that have not averaged out due to the finite length of the observation series, the second is caused by systematic errors of the probe. Based on the calibration, we believe that the systematic error is less than 0.005 m s^{-1} for the hot wires, and less than 0.1 Pa for the pressure probe. The uncertainty in the Reynolds stress components due to the systematic error in the hot wire is estimated as $4\Delta U u_*$, where ΔU is the systematic error of the hot wire. The friction velocity u_* is used as a measure of the turbulent fluctuations in the velocity observations. From (2.5) follows that the error in the components of the amplitude $\hat{q}$ is $\sqrt{2}$ of the error in the mean. In the figures presented in this paper, the error bars indicate the maximum of the random error and the estimated systematic error. For the amplitudes of the horizontal and vertical velocity components the contribution of the random error dominates; for the Reynolds stresses and the pressure amplitudes the limited accuracy of the probes determines the accuracy.

3. The numerical model

The velocity and pressure distribution of the air flow over waves is governed by the Reynolds-averaged Navier–Stokes equations for an incompressible fluid:

$$\frac{\partial \bar{u}_i}{\partial t} + \bar{u}_j \frac{\partial \bar{u}_i}{\partial x_j} = -\frac{1}{\rho_a}\frac{\partial \bar{p}}{\partial x_i} - \frac{\partial \overline{u'_i u'_j}}{\partial x_j}, \tag{3.1}$$

$$\frac{\partial \bar{u}_i}{\partial x_i} = 0. \tag{3.2}$$

Here the overbar denotes an ensemble average, $\bar{u}_i$, $i = 1, 2, 3$, are the Reynolds-averaged velocity components of the air flow, t is time, x_i, $i = 1, 2, 3$, are the spatial coordinates, ρ_a is the density of air, $\bar{p}$ is the Reynolds-averaged pressure and $\overline{u'_i u'_j}$, $i, j = 1, 2, 3$, are correlations that give rise to Reynolds stresses. (Throughout the article repeated indices imply a summation, and two equivalent notations for both the spatial coordinates $(x, y, z) = (x_1, x_2, x_3)$ and velocities $(u, v, w) = (u_1, u_2, u_3)$ are used.) The air is assumed to be flowing over a second-order Stokes wave propagating along the x-axis:

$$\eta(x, t) = a\cos(kx - \omega t) + \tfrac{1}{2}ka^2(1 + \cos(2kx - 2\omega t)), \tag{3.3}$$

where $\eta(x, t)$ is the elevation, a is the amplitude of the wave, k is the wavenumber and ω is the angular frequency. The orbital velocities u_{0i} of this wave are used as lower boundary conditions at $z = \eta(x, t)$ for the air flow. At the top of the domain $z = h$ we prescribe a constant horizontal wind speed U_h, and we set the vertical velocity to zero.

Since none of the boundary conditions depends on the y-coordinate, neither will the solution. So the numerical model needs to take into account only two spatial coordinates: x and z. All derivatives with respect to y appearing in (3.1) and (3.2) can be ignored. In the present study we only consider waves going in the same direction as the wind, which means that the equation for v can be eliminated.

3.1. *The turbulence closure schemes*

Before the four equations (3.1) and (3.2) can be solved for $\bar{u}_i$ and $\bar{p}$, expressions for the Reynolds stress terms have to be supplied. In the model described here, three different closure schemes are used. Two of these, the mixing length and the e-ϵ schemes, are based on the concept of eddy viscosity. In the third, dynamical equations for the second-order correlations $\overline{u'_i u'_j}$ are solved, using parameterizations for third-order correlations that appear in these equations.

3.1.1. *Mixing length*

In analogy with the molecular viscosity, the eddy viscosity is introduced by assuming that the traceless part of the Reynolds stress tensor $-\rho_a \overline{u_i' u_j'}$ is proportional to the rate of strain tensor. The resulting relation is known as the closure hypothesis of Boussinesq:

$$-\overline{u_i' u_j'} + \tfrac{2}{3} e \delta_{ij} = 2K S_{ij}, \tag{3.4}$$

where K is the eddy viscosity and e is the turbulent kinetic energy:

$$e = \tfrac{1}{2}\overline{u_i' u_i'}. \tag{3.5}$$

The symmetrical rate of strain tensor S_{ij} is defined as

$$S_{ij} = \frac{1}{2}\left(\frac{\partial \bar{u}_i}{\partial x_j} + \frac{\partial \bar{u}_j}{\partial x_i}\right). \tag{3.6}$$

In the simplest of the three turbulence schemes we consider, the eddy viscosity K is itself also a function of the local rate of strain, and of the height z above the surface:

$$K = (\kappa z)^2 (2 S_{ij} S_{ij})^{1/2}, \tag{3.7}$$

where $\kappa \simeq 0.41$ is the von Kármán constant. The closure hypothesis (3.4) in combination with (3.7) is called the mixing length scheme. Note that this turbulence parameterization does not allow the calculation of the turbulent kinetic energy e. By redefining pressure as $\bar{p} + 2e/3$ the turbulent kinetic energy is eliminated from the equations, and the resulting set of equations is closed.

3.1.2. *The e-ϵ model*

This scheme also uses the Boussinesq closure hypothesis (3.4), but differs in the parameterization of the eddy viscosity K. Unlike in the mixing length model, the eddy viscosity is now a function of the turbulent kinetic energy e and the dissipation rate ϵ (hence the name e-ϵ model):

$$K = c_\mu \frac{e^2}{\epsilon}, \tag{3.8}$$

where c_μ is a dimensionless constant. The turbulent kinetic energy e and the dissipation rate ϵ are calculated dynamically:

$$\frac{\partial e}{\partial t} + \bar{u}_i \frac{\partial e}{\partial x_i} = -\frac{\partial \overline{e' u_i'}}{\partial x_i} - \frac{1}{\rho_a}\frac{\partial \overline{p' u_i'}}{\partial x_i} + P - \epsilon, \tag{3.9}$$

$$\frac{\partial \epsilon}{\partial t} + \bar{u}_i \frac{\partial \epsilon}{\partial x_i} = -\frac{\partial \overline{\epsilon' u_i'}}{\partial x_i} + \frac{\epsilon}{e}(c_{1\epsilon} P - c_{2\epsilon}\epsilon), \tag{3.10}$$

where P is the production of turbulent kinetic energy:

$$P = -\overline{u_i' u_j'}\frac{\partial \bar{u}_i}{\partial x_j}, \tag{3.11}$$

and the turbulent fluxes are parameterized as

$$\overline{e' u_i'} + \frac{1}{\rho_a}\overline{p' u_i'} = -\frac{K}{\sigma_e}\frac{\partial e}{\partial x_i}, \tag{3.12}$$

$$\overline{\epsilon' u_i'} = -\frac{K}{\sigma_\epsilon}\frac{\partial \epsilon}{\partial x_i}. \tag{3.13}$$

In this study we use the standard values for the five dimensionless constants in the e-ϵ model (Jones & Launder 1972): $c_{1\epsilon} = 1.44$, $c_{2\epsilon} = 1.92$, $c_\mu = 0.073$, $\sigma_e = 1.0$ and $\sigma_\epsilon = 1.3$.

3.1.3. *The second-order model*

In a second-order model the dynamical equations for the second-order correlations are solved. Like the Reynolds equations, the equations for the second-order correlations follow from the Navier–Stokes equations combined with a (Reynolds) averaging procedure. This set of equations will contain third-order correlations, which need to be expressed in known quantities in order to get a closed set of equations. In this work we use the parameterization introduced by Launder, Reece & Rodi (1975), hence we refer this scheme as the LRR second-order scheme. The balance equations for the six independent correlations $\overline{u_i'u_j'}$ read

$$\frac{\partial \overline{u_i'u_j'}}{\partial t} + \bar{u}_k \frac{\partial \overline{u_i'u_j'}}{\partial x_k} = P_{ij} + T_{ij} + \Pi_{ij} - \epsilon_{ij}, \tag{3.14}$$

where the right-hand-side terms represent the production, the turbulent diffusion, the work of pressure–velocity correlations and the molecular dissipation. In the Appendix the expressions used for the right-hand-side terms are given.

3.2. *Discretization and solution technique*

To simplify the solution of the equations, the coordinates (x, z) are expressed in terms of (χ, ξ), where $\chi = (kx - \omega t)/2\pi$ and $\xi = (z - \eta)/(h - \eta)$. The domain is now $0 \leqslant \chi, \xi \leqslant 1$. The velocities and stresses are not transformed. In the new coordinate system the surface is stationary and since we impose a constant wind velocity at the top, the solution of the equations will also be stationary. In Makin (1979) and Burgers & Makin (1993) the governing equations are given in the transformed coordinate system (χ, ξ).

The resolution close to the surface is increased by discretizing the vertical coordinate as

$$\xi_j = \frac{\gamma^j - 1}{\gamma^m - 1}, \qquad j = 0, 1, \ldots, m, \tag{3.15}$$

where γ is the vertical stretching parameter and m is the number of layers in the vertical. Starting from the surface ($j = 0$), the spacing between the vertical layers increases by a factor γ per layer. The lowest model layer ξ_1 has to be within the so-called inner surface layer (ISL) (Belcher & Hunt 1993). In this layer, located within the inner region, the wave-induced stresses are no longer height dependent. In figure 2 an overview is given of the vertical structure of the flow as a function of U_λ/C. The depth δ of the ISL depends on the depth l of the inner region: $\delta \simeq (lz_o)^{1/2}$, where the depth of the IR is given by the implicit relation $kl = 2\kappa u_*/|U_l - c|$, where U_l is the mean wind speed at the top of the inner region l (see also the discussion below (4.5)). The smaller kz_0, the lower the first model layer has to be located. This can be achieved by increasing the stretching parameter γ or by increasing the number of layers in the vertical. Both options give rise to an increase in computation time. For $kz_0 = 10^{-4}$ the vertical domain of the numerical model spans roughly three orders of magnitude: from the top of the ISL at $kz \simeq 4 \times 10^{-2}$ to $kz = 2\pi$. For dimensionless roughnesses smaller than 10^{-5} the computation time becomes impractically long. To simulate the air flow over a wave with roughness $kz_0 = 10^{-4}$ typically 80 layers in the vertical are used, with a 6% increase in spacing per vertical layer ($\gamma = 1.06$). The

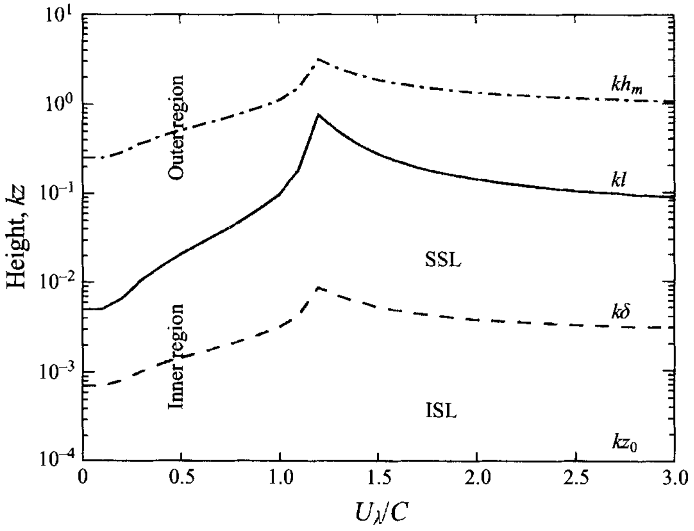

FIGURE 2. Overview of the vertical structure of the flow over waves as a function of U_λ/C. The dimensionless surface roughness is kept constant at $kz_0 = 10^{-4}$. The solid line indicates the depth kl of the inner region. The depth $k\delta$ of the inner surface layer (ISL) is shown as a dashed line. The remaining part of the inner region is called the shear stress layer (SSL).

lowest layer is then located at $kz = 3 \times 10^{-3}$, roughly at the top of the ISL. A further increase of the resolution does not change the results.

The grid is staggered: the pressure and the stresses are calculated at half grid points, centred between four velocity points.

The model uses a standard finite difference scheme, with second-order accuracy in both space and time. The difference with results from a time step with first-order accuracy is used to estimate the optimal size of the next time step. The elliptical equation for pressure is solved with the successive over-relaxation (SOR) method using Chebyshev acceleration.

3.3. *The boundary conditions*

At the air–sea interface the orbital velocities u_0, w_0 and the surface roughness distribution $z_0(x)$ is given. Surface values for the e and the second-order moments are calculated from the tangential stress at the surface using their equilibrium values. The bottom boundary condition for the ϵ-equation is provided by putting the vertical gradient to its equilibrium value:

$$\frac{\partial \epsilon}{\partial z} = -\frac{u_*^3}{\kappa z^2}. \tag{3.16}$$

The tangential stress at the surface is calculated from the velocity, assuming the tangential velocity profile is logarithmic with height between the surface and the first model layer. This assumption is also used to calculate the tangential velocity gradients, since the standard finite difference formula is inaccurate owing to the large velocity gradient between the surface and the first model level.

We impose periodic boundary conditions in the x-direction. The height h of the domain is set equal to the length of the wave $\lambda = 2\pi/k$. At this height the wave-induced properties are small enough to be ignored. The velocities at the top of the domain are prescribed: the horizontal u_λ forces the flow, and the vertical velocity w_λ

is set to zero. The upper boundary conditions for e and the turbulent moments are found by setting their vertical gradients to zero at the top. The vertical gradient of the dissipation ϵ is assumed to be inversely proportional to the height squared.

The water wave is assumed to be a gravity wave in deep water, for which the dispersion relation $\omega^2 = gk$ is valid, where g is the gravitational acceleration. The system is completely determined by specifying the following parameters: the wind speed U_λ at height λ, the wavenumber k, the amplitude a, the surface roughness z_0 and the gravitational acceleration g. If we replace g by the phase speed $c = (g/k)^{1/2}$, we find that the system is determined by the three dimensionless variables U_λ/c, ak, and kz_0. When we want to calculate the growth rate of the wave (see below), the ratio of the density of air and water ρ_a/ρ_w enters as a proportionality factor. We conclude that in the numerical model presented here, the growth rate is a function of four dimensionless parameters. One of these dependencies, on the density ratio, is trivial since it factorizes.

4. Effects of turbulence closure on wave growth

The choice of the turbulence scheme has a large impact on the results for the energy flux from wind to waves. Not only does the growth rate change quantitatively, but also its dependence on the parameters mentioned above changes. Before discussing these changes and their cause, first the numerical model is validated by comparing results for air flow over hills, which is closely related to the subject of this paper.

4.1. *Validation of the model*

To validate the model the drag caused by a periodic sinusoidal hill is calculated, and compared with results from calculations presented in Belcher *et al.* The boundary conditions for a hill can be obtained by putting $\omega = 0$ in (3.3), and by putting the orbital velocities to zero. We will compare calculations of the dimensionless form drag S, defined as

$$S = \frac{2\pi \langle p\eta_x \rangle_{z=\eta}}{\rho_a u_*^2 (ak)^2}, \tag{4.1}$$

where $\eta_x = \partial\eta/\partial x$. The dimensionless form drag for flow over hills is the equivalent of the growth rate parameter in the case of waves. In figure 3 the sheltering coefficient is presented as a function of kz_0. Results from all three turbulence parameterizations are compared, both with other numerical models and with analytical calculations. The agreement between the results from the numerical model presented here and the other numerical models is excellent. The analytical results for the mixing length closure are obtained with the van Duin & Janssen model, modified to include also the effect of the wave-induced stress in the inner region (see discussion in Belcher, Harris & Street 1994, and in Wood & Mason, 1993). The analytical model of Belcher *et al.* (1993) should be comparable with results from the second-order closure schemes, since both take into account that the turbulence in the outer region is distorted rapidly. As can be seen in figure 3, this is indeed the case for small roughnesses. For larger roughnesses, $kz_0 > 10^{-3}$, the analytical model yields larger sheltering coefficients than both numerical models. In the analytical approach of Belcher & Hunt (1993), the solution of the equations is found under the assumption that the inner region is thin. As will be shown below, see equation (4.7), the depth of the inner region increases with the dimensionless roughness kz_0. For $kz_0 > 10^{-3}$ the breakdown of the assumption

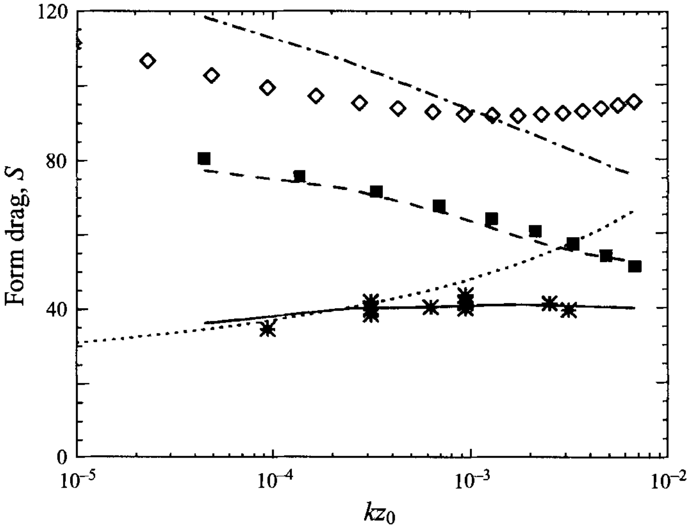

FIGURE 3. The form drag of a hill S as a function of the surface roughness kz_0. The lines indicate results obtained with the numerical model used in this paper: solid line, LRR turbulence scheme; dashed line, e-ϵ scheme; dashed-dotted line, mixing length scheme. The symbols indicate form drags calculated with different models: dots, analytical model of Belcher *et al.* (1993); astrisks, numerical model of Belcher *et al.* (1993) with LRR turbulence model; solid squares, undamped e-ϵ model of Harris *et al.* (1995); open diamonds, analytical model of van Duin and Janssen (1993) modified by Belcher *et al.* (1994) using a mixing length closure.

that the inner region is thin becomes a major source of error in the analytical theory.

4.2. *The energy flux to waves*

The energy flux due to surface stresses to a wave with energy E per unit area is given by:

$$\dot{E}_{wind} = \langle \tau_\perp u_\perp \rangle_{z=\eta} + \langle \tau_\parallel u_\parallel \rangle_{z=\eta}, \tag{4.2}$$

where the average $\langle\rangle_{z=\eta}$ is performed along the surface of the wave η, which corresponds to $\xi = 0$ (see also the discussion below equation (5.2)). Transforming the normal and tangential stresses and velocities to the Cartesian frame of reference used in the model yields

$$\dot{E}_{wind} = \frac{1}{\lambda}\int_0^\lambda \left\{ \underbrace{-p(w_0 - \eta_x u_0)}_{\text{(i)}} \underbrace{-\rho_a(\overline{w'w'}w_0 - \overline{u'u'}\eta_x u_0)}_{\text{(ii)}} \underbrace{-\rho_a\overline{u'w'}(u_0 - \eta_x w_0)}_{\text{(iii)}} \right\} \mathrm{d}x. \tag{4.3}$$

Following Belcher & Hunt (1993) the energy flux is separated into three parts, where for the different parts the work is done by (i) the pressure, (ii) the velocity variances or (iii) the shear stress. The relative contributions of these three terms is discussed below. The growth rate due to the wind is defined as $\gamma = (1/E)\dot{E}_{wind}$. The energy of a gravity wave is taken to be $E = \rho_w g\langle\eta^2\rangle$. Following Miles (1957) and Townsend (1972), growth rates will be presented in terms of the parameter β, defined as

$$\frac{\gamma}{\omega} = \beta\frac{\rho_a}{\rho_w}\left(\frac{u_*}{c}\right)^2. \tag{4.4}$$

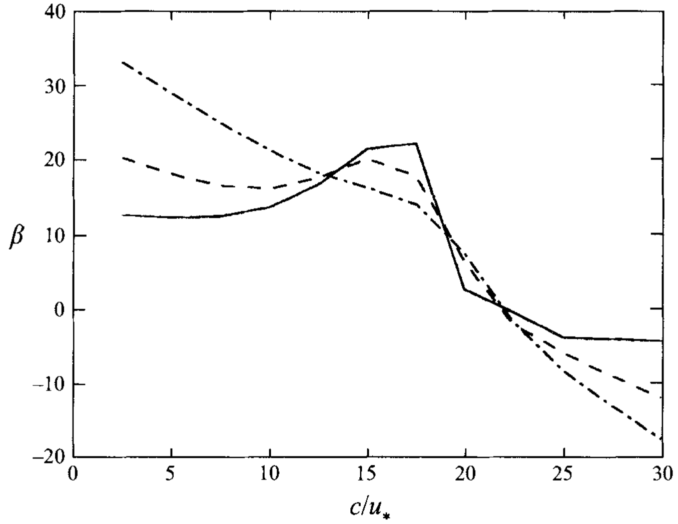

FIGURE 4. The growth rate parameter β *vs.* the ratio c/u_* calculated with the numerical model using three different closures: dash-dot, mixing length; dashed, the e-ϵ scheme; solid line, the LRR model. The dimensionless roughness $kz_0 = 10^{-4}$.

Based on a compilation of experimental data from various sources, Plant (1982) concluded that for waves slow compared to the wind $\beta = 32 \pm 16$.

The growth rate calculated with the numerical model depends strongly on the type of turbulence closure used. In figure 4 the growth rate parameter β is shown as a function of the ratio c/u_* for waves with a dimensionless roughness of $kz_0 = 10^{-4}$. For waves slow compared to the wind ($c/u_* < 13$, or equivalently $U_\lambda/c > 2$) the mixing length scheme yields much larger growth rates than the LRR model. The decay rate for waves going faster than the wind ($c/u_* > 22$, $U_\lambda/c < 1.2$) is also reduced in the Reynolds stress model. However, for waves just slower than the wind ($1.4 < U_\lambda/c < 2$) the growth rate is enhanced in the Reynolds stress model. In all three regimes the growth rate calculated with the e-ϵ scheme is located between the results from the mixing length model and the Reynolds stress model. Note that for slow waves β calculated with the Reynolds stress model is almost independent of the ratio c/u_*, consistent with the experimental data presented by Plant (1982). The same result is reported by Townsend (1972) and Belcher & Hunt (1993). However, all these models underestimate the value proposed by Plant by a factor more than 2.

In table 1 the relative contributions of the parts (i) to (iii) denoted in equation (4.3) are listed for a slow moving wave $U_\lambda/c = 5$, a fast moving wave ($U_\lambda/c = 1.5$) and a wave propagating faster than the wind ($U_\lambda/c = 0.80$). For slow waves, $U_\lambda/c > 2.7$, all contributions to the energy flux are positive, and the contribution from the pressure is dominant. When the ratio U_λ/c drops below this value, the work of the tangential stress on the orbital velocities, contribution (iii), becomes negative. Owing to the work of the pressure the total energy flux to the waves remains positive as long as $U_\lambda/c > 1$. When the ratio U_λ/c drops below 1, the contribution due to the pressure perturbation is no longer dominant. The negative energy flux for these waves is maintained mainly by the work of the shear stress on the orbital velocities (contribution (iii)).

U_λ/c	c/u_*	β	(i)	(ii)	(iii)
5.0	5.3	14.5	78%	10%	12%
1.5	18.0	21.7	104%	5%	−8%
0.8	33.0	−5.6	11%	7%	82%

TABLE 1. Contributions to the energy flux using the LRR model. The dimensionless roughness $kz_0 = 10^{-4}$.

4.3. *Turbulence in the outer region*

The reason for the large differences in growth rate between the three turbulence closure schemes can be understood with a physical scaling argument regarding the response of turbulence to a rapidly changing forcing. This scaling argument is discussed at length in Belcher *et al.* (1993). An eddy advected over a wave experiences changes in velocity shear at a timescale that is proportional to the time it takes the eddy to pass over a wave:

$$T_D \sim \frac{\lambda}{|U_z - c|}. \tag{4.5}$$

The timescale on which the eddy can adjust itself to changes in the shear is believed to be proportional to the eddy turnover time, which is equal to the ratio of the typical size of the eddy to the friction velocity. The typical size of eddies in a boundary layer is κz, so it follows that the timescale of eddie adjustment to a change in the forcing is proportional to the height above the surface:

$$T_L \sim \frac{\kappa z}{u_*}. \tag{4.6}$$

For waves with a phase speed smaller than the wind speed, the vertical domain is now divided into two regions: the *inner region*, where $T_L < T_D$, and the *outer region*, where $T_L > T_D$. An estimate of the depth of the inner region can be found from (4.5) and (4.6) by putting $T_L \sim T_D$. For historical reasons (Jackson & Hunt, 1975) the $O(1)$ proportionality constant is chosen such that

$$kl = 2\kappa \frac{u_*}{|U_l - c|}. \tag{4.7}$$

In the inner region, $z < l$, the turbulence is in local equilibrium with the velocity shear. At each point the production of turbulent kinetic energy is balanced by the dissipation. It follows that an eddy viscosity closure scheme of the type (3.4) can be used to model the stress in this region. In the outer region, $z > l$, the eddies are distorted more rapidly than they can react, and they will not be in local equilibrium with the shear. Turbulent kinetic energy will be advected away from regions with excess production, before a local balance with the dissipation can be reached. The eddy viscosity hypothesis, which implies local equilibrium, no longer holds. A second-order Reynolds stress model, like the LRR scheme, incorporates advection of turbulent moments. Therefore it is expected that this turbulence scheme should be able to cope with this aspect of rapidly distorted turbulence.

The modification of the turbulence in the outer region is described by rapid distortion theory (Batchelor & Proudman *et al.* 1954). In Britter *et al.* (1981), Zeman & Jensen (1987) and Belcher *et al.* (1993) detailed descriptions of the effects of rapid distortion on turbulence in the outer region can be found. Their conclusions are that, owing to the irrotational straining of the initially anisotropic turbulence, the horizontal velocity variance $\overline{u'u'}$ is reduced above the crest. The effect on $\overline{w'w'}$ depends on the anisotropy $A = \overline{u'u'}/\overline{w'w'}$ of the mean flow: if $A < 3$ the vertical velocity variance $\overline{w'w'}$ is reduced owing to the irrotational strain effect, for $A > 3$ the effect reverses sign. The curvature of the mean streamlines in the outer region rotates the stress tensor. Zeman & Jensen (1987) find that this effect is important at the top of the inner region. A part of the observed reduction of the shear stress above the top of the Askervein hill could be attributed to the curvature effect. The ability of second-order models like the LRR scheme to reproduce rapid distortion effects depends on the parameterization of the rapid term $\Pi^{(2)}$. Though the LRR model gives the right sign and order of magnitude of both rapid effects, alternatives to the LRR parameterization exist, and they may yield different results. A comparison of such parameterizations with direct numerical simulations can be found in Shih & Lumley (1993).

4.4. *The relation between growth rate and turbulence model*

As can be seen in figure 4, the growth rate for slow waves calculated with the mixing length scheme is significantly larger than the one following from the LRR closure, with the growth rate from the e-ϵ scheme in between. As shown in detail in Belcher *et al.* (1993), this is a direct consequence of the difference in handling the rapidly distorted turbulence in the outer region. Since the link between turbulence models and growth rates is a central issue of this paper, their analysis will be briefly recaptured here.

In Belcher *et al.* (1993) it is shown that in the *upper layer* of the outer region the wave-induced flow is potential. In the lower part of the outer region the wave-induced flow is also inviscid, but rotational. The upper layer starts at the height h_m:

$$kh_m = \left(\frac{u_*}{\kappa U_m}\right)^{1/2} \tag{4.8}$$

(Belcher and Hunt, 1993) where U_m is the mean windspeed at level h_m. It follows that the velocity perturbations in this layer can be written as:

$$\tilde{u} = \mathrm{Re}[u_m e^{ikx-kz}], \tag{4.9}$$

$$\tilde{w} = \mathrm{Re}[iu_m e^{ikx-kz}]. \tag{4.10}$$

Here u_m is the complex amplitude of the wave-induced velocities at the bottom of the upper layer. For the eddy viscosity closures the Reynolds stress perturbation follows from the Boussinesq hypothesis:

$$\tilde{\tau}/\rho_a = 2\tilde{K}\langle S_{xz}\rangle + 2\langle K\rangle\tilde{S}_{xz}. \tag{4.11}$$

If the velocity perturbations (4.9) and (4.10) are substituted in the equations (3.6) and (3.7) that enter (4.11), an expression for the stress perturbation $\tilde{\tau}$ in terms of u_m can be found when the mixing length scheme is used. The mixing length scheme gives a stress perturbation that is 180° out-of-phase with the velocity perturbations. To calculate the impact of the stress perturbation on the out-of-phase pressure component, the linearized vertical momentum equation has to be integrated from infinity down to h_m:

$$\mathrm{Im}[\hat{p}_m] = \rho_a \int_{h_m}^{\infty} (U_z - c)\mathrm{Re}[\hat{w}]k\mathrm{d}z - \int_{h_m}^{\infty} \mathrm{Re}[\hat{\tau}]k\mathrm{d}z. \tag{4.12}$$

The first term on the right-hand side represents the contribution to the growth of an undulating flow that is shifted in phase with respect to the wave. In terms of the potential flow approximation (4.9) and (4.10) this contribution is proportional to the imaginary part of the wave-induced velocity perturbation at the bottom of the upper layer. Due to the second term on the right-hand side of equation (4.12) the wave-induced Reynolds stress $\tilde{\tau}$ has a direct impact on the wave growth. The Reynolds stress perturbation in the upper layer calculated with the mixing length scheme will contribute

$$\beta^{mix} = 4\frac{\mathrm{Re}[u_m]}{akU_m}\frac{\kappa U_m}{u_*}(1 + O(\varepsilon^{1/2})), \tag{4.13}$$

where $\varepsilon = u_*/\kappa U_m$ is believed to be small. The total growth rate will include contributions of the stress modulation in the inner region and the rest of the outer region, and from the term involving $\mathrm{Re}[\hat{w}]$ in equation (4.12).

In the LRR model, the velocity perturbations (4.9) and (4.10) modulate the production terms. In the outer region the advection terms will balance this modulation. This results in a modulation of the shear stress that is reduced by a factor ε compared to the mixing length result. The contribution to the growth rate of the stress modulation in the LRR model is

$$\beta^{LRR} = -4\frac{\mathrm{Im}[u_m]}{akU_m}\frac{e}{3u_*^2}(1 + O(\varepsilon^{1/2})). \tag{4.14}$$

Even if $\mathrm{Im}[u_m] = \mathrm{Re}[u_m]$, meaning that the undulating flow in the outer region is 45° out-of-phase with the wave, the contribution of equation (4.14) is smaller than (4.13) by a factor of ε.

In the mixing length model, both terms in equation (4.11) contribute equally to the stress modulation. In the e-ϵ scheme, where the eddy viscosity K is calculated from the dynamical variables e and ϵ, the modulation of the eddy viscosity will be suppressed. This leaves only the second term in equation (4.11) to modulate the stress. It follows that the contribution to the wave growth of stress contributions in the outer region in the e-ϵ scheme will be half that of the mixing length scheme.

5. Comparison of the observations with model results

5.1. *Procedure*

The parameters for the three sets of observations are listed in table 2. To simulate these experiments with the numerical model, four quantities need to be specified: the wavelength λ, the amplitude a, the wind speed U_λ and the surface roughness z_0. The first two are easily obtained from the observations. The surface roughness z_0 and the wind speed U_λ are determined by fitting a logarithmic profile through the observed mean wind speeds using a least-squares method.

The observations are performed at a fixed height above the mean water level. Necessarily the average $\langle\rangle$ over a wavelength for the observations has to be performed for constant z. In the numerical model the (Cartesian) velocities, pressure, stresses and variances are calculated on the wave-following (χ, ξ)-grid. To comply with the procedure followed with the observations, the results are transformed to the (x, z)-frame (using linear interpolation between the grid points) before they are decomposed into mean and wave-induced parts. From the wave-induced properties a complex amplitude of the first harmonic is determined with the help of (2.5).

The velocities in the plots are normalized with the wind speed in the middle of the wave flume U_∞, velocity variances with u_*^2 and the stress τ and the pressure p with

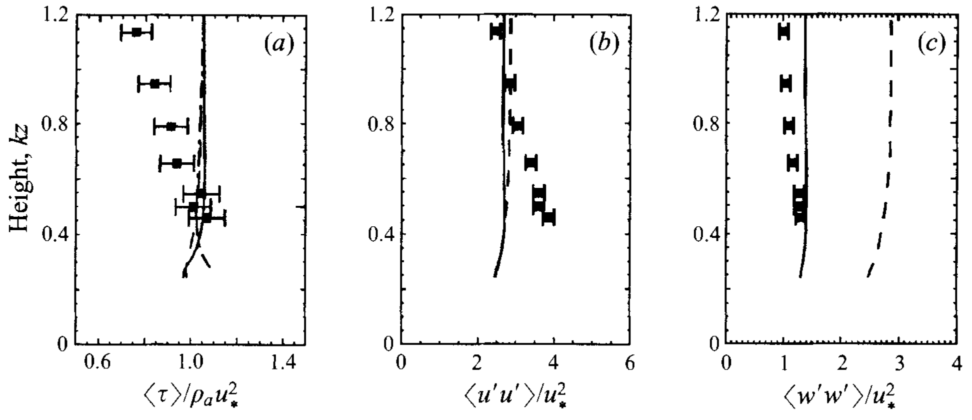

FIGURE 5. Profiles of mean turbulent stress components for run 35: the mean stress $\langle\tau\rangle$, (*b*) the horizontal velocity variance and (*c*) the vertical velocity variance. Model results with different turbulence closures are also shown: dash-dotted line, mixing length; dashed line, e-ϵ; solid line, LRR turbulence scheme.

Run	U_∞ (m s^{-1})	u_* (m s^{-1})	λ (m)	ak	N_h	U_λ/c	c/u_*	kz_0	kl
35	6.3	0.26	0.80	0.18	7	5.3	4.3	5.5×10^{-4}	0.10
BA	5.4	0.21	0.80	0.15	9	4.6	5.3	2.9×10^{-4}	0.09
B2	3.5	0.15	0.92	0.09	5	2.8	8.0	6.5×10^{-4}	0.27

TABLE 2. Parameters for the three sets of observations. The friction velocity u_* is determined from the mean velocity profile. N_h is the number of heights at which observations were made. In the last column the dimensionless depth kl of the inner region is given.

$\rho_a u_*^2$. The wind speed U_∞ and the friction velocity u_* can be found in table 2, for the density of the air ρ_a the value 1.3 kg m^{-3} is used. Additionally, (amplitudes of) wave induced quantities are normalized with the steepness of the paddle wave ak, which is also listed in table 2.

5.2. *Comparison*

The friction velocity derived from the mean velocity profile is in good agreement with the observed stress $\langle\tau\rangle = -\rho_a\langle\overline{u'w'}\rangle$. This can be seen in figure 5, where profiles of the horizontal velocity, stress and velocity variances for run 35 are shown. The stress values, normalized with the friction velocity obtained from the velocity profile, are scattered around unity. In all sets, the stress is decaying with height, which is a consequence of the horizontal pressure gradient that is forcing the wind in the wave flume. The mean variance of the observed horizontal velocity $\langle\overline{u'u'}\rangle$ also decays with height, but the variance of the vertical velocity is constant with height. The anisotropy in the velocity variances is reasonably reproduced by the LRR model, though the horizontal velocity variance $\langle\overline{u'u'}\rangle$ close to the surface is underestimated. The e-ϵ scheme, which gives $\langle\overline{u'u'}\rangle \simeq \langle\overline{w'w'}\rangle \simeq 2e/3$, overestimates the vertical velocity variance by a factor 2 compared to the observations. Since the mixing length scheme does not provide the turbulent kinetic energy e, the horizontal and vertical velocity variances cannot be calculated with this scheme.

Figures 6 and 7 show a comparison between the observed and modelled wave-induced pressure and velocities at a constant height. For sets 35 and BA (the latter is not shown) the prescribed Stokes wave is in good agreement with the observed phase-averaged elevations, except near the crests where the wave seems to be pushed forward relative to the Stokes profile (solid line). For the set with the longest wave and the smallest amplitude, B2, the wave shape is slightly distorted. The departure of the pressure and velocity perturbations from a sinusoidal shape is well captured by the numerical simulation. To find out whether the Stokes profile (3.3) or the nonlinearity of the equations of motion of the air are responsible for the asymmetrical perturbations, two additional calculations were performed. In the first, a sinusoidal wave of the same steepness as the laboratory wave is used as a bottom boundary condition (dashed lines in figure 6); in the second calculation the steepness is reduced by a factor 10 (dash-dotted lines). From the figures we can conclude that the Stokes profile is responsible for an extra speed-up over the crest, which is associated with an extra-deep minimum in the pressure perturbation. The nonlinearity of the equations manifests itself mainly by reducing the deceleration of the flow in the trough, limiting the maximum of the pressure perturbation. Both effects seem to be of equal importance to the asymmetry of the vertical velocity perturbation.

The observations of the pressure and velocities in the set with the lowest wind speed, B2, show much more scatter than in the other two sets. This may be explained by the fact that the wave-induced velocities, which scale with akU_∞, are approximately 4 times smaller for this set, since both the steepness ak and the wind speed U_∞ are a factor 2 smaller. This reduces the signal to noise ratio also by a factor 4, which is reflected by the relatively large error bars in figure 7. The wave-induced pressure and velocity correlations are even a factor 8 smaller for this set, since they scale with aku_*^2.

The phase shifts in the pressure observed in runs 35 and BA imply that the bulk of the momentum passes along the surface via the paddle waves. If we assume that most of the work on the wave is done by the out-of-phase component of the pressure, the fraction of the momentum flux supported by the paddle wave is (Townsend 1972):

$$\frac{\tau_w}{\langle\tau\rangle} = \tfrac{1}{2}(ak)^2\beta. \tag{5.1}$$

Extrapolating the observed amplitudes of the out-of-phase component of the pressure to the surface we find that for run 35 the paddle wave is responsible for 80% of the momentum flux, and for 55% in the case of run BA. If such large fractions of the downward momentum flux are supported by organized wave-induced motions, the turbulent momentum flux close to the surface must be significantly reduced. As the growth rate of slow waves is coupled to the surface stress (Plant 1982), this means that paddle waves are able to suppress the growth of wind ripples in wind-wave tanks. The fact that the presence of paddle waves seems to reduce the level of wind ripples has been observed both in the IRPHE wind tunnel, and in others (e.g. Donelan, 1987).

The profiles of the amplitudes of the wave-induced velocities, see figure 8, show that the numerical model reproduces well the real part of the horizontal amplitude Re[$\hat{u}$] and the imaginary part of the vertical velocity Im[$\hat{w}$]. This is the part of the undulating flow in phase with the wave. Owing to the work of stresses close to the surface the phase of the undulating flow is shifted downwind, giving rise to non-zero values for Im[$\hat{u}$] and Re[$\hat{w}$]. The numerical simulations show a smaller shift downwind of the undulating flow than the observations. This picture is consistent with the observations of the pressure perturbations. The real part of the amplitude

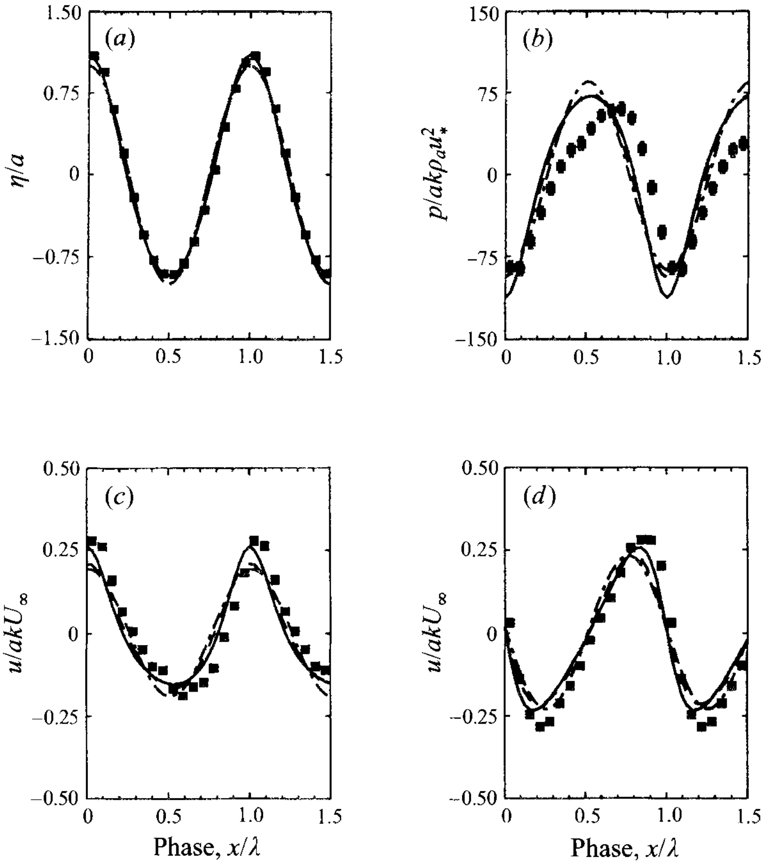

FIGURE 6. (a) Phase-averaged elevation, (b) pressure, (c) the horizontal and (d) the vertical velocity components for run 35 ($U_\lambda/c = 5.3$). The pressure and velocity are measured at a height $kz = 0.46$. Results with the LRR are also shown: dash-dotted line, reduced amplitude ($ak = 0.018$); dashed line, sinusoidal wave ($ak = 0.18$); solid line, Stokes wave ($ak = 0.18$).

of the pressure variation Re[$\hat{p}$] is slightly overestimated in the numerical simulations. However, the imaginary part of the pressure amplitude is underestimated by a factor 2 to 4, depending on the closure scheme. So both the velocity and the pressure observations indicate that the numerical model reproduces reasonably the in-phase part of the undulating flow, but it underestimates the out-of-phase part.

The differences between the three closure schemes used in the numerical model are most apparent in the amplitudes of the Reynolds stress variations (figures 9 and 10). As expected on the basis of the physical scaling argument given above, the mixing length model overestimates the real part of the stress amplitude. In the LRR closure the amplitude in this part of the vertical domain is reduced by more than an order of magnitude. For all three runs, the observations show an equally small amplitude. The amplitudes obtained with the e-ϵ scheme, roughly one third of the mixing length amplitudes, are still significantly larger than the observed values.

The imaginary parts of the amplitudes of the velocity variances $\overline{u'u'}$ and $\overline{w'w'}$ calculated with the LRR scheme show a better agreement with the observations than the results obtained with the e-ϵ scheme. As the observed anisotropy A is smaller than 3, rapid distortion theory implies that the irrotational straining of anisotropic

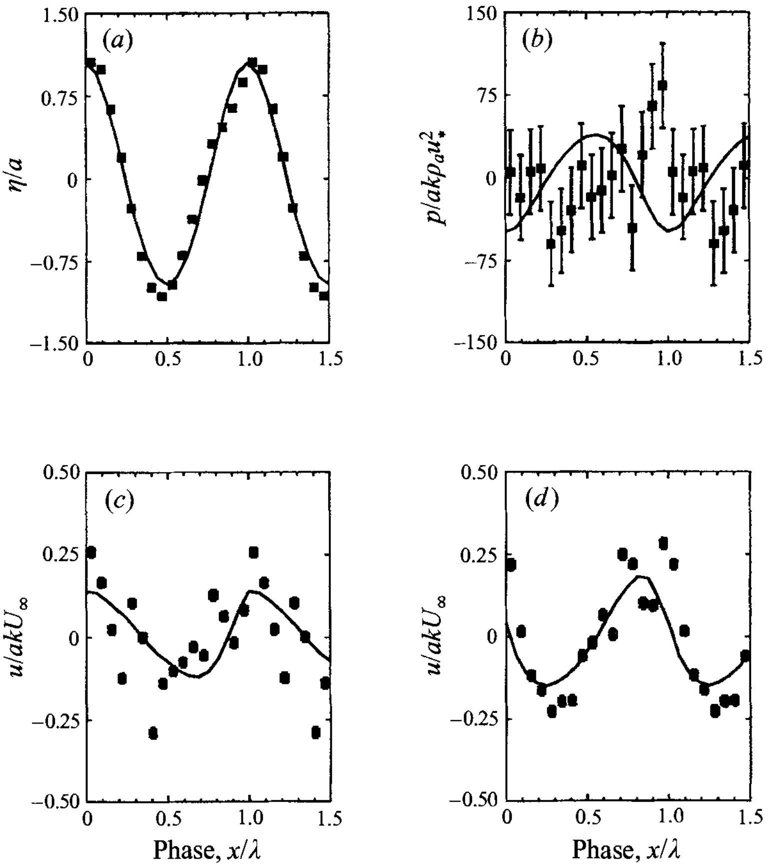

FIGURE 7. As figure 6 but for run B2 ($U_\lambda/c = 2.8$). The pressure and velocity are measured at a height $kz = 0.22$.

turbulence should decrease both $\mathrm{Re}[\overline{u'u'}]$ and $\mathrm{Re}[\overline{w'w'}]$. Compared to the (isotropic) e-ϵ model, the LRR scheme is doing just that. The uncertainties in the observed variances obscure this effect, except perhaps in the lowest observations of $\mathrm{Re}[\overline{w'w'}]$ in run BA, where a significant increase is observed that is not present in the model calculations.

Far from the surface the vertical momentum flux is maintained by the Reynolds stress $\tau_t = -\rho_a \overline{u'w'}$. Close to the surface correlations of the more organized wave-induced motions also contribute to the momentum flux. In Cartesian coordinates this flux is equal to $\tau_w = -\rho_a \langle \tilde{u}\tilde{w} \rangle$, where the averaging is performed for constant z. Since this flux is not defined for heights smaller than the amplitude of the wave, it is convenient to define a flux going through a plane that follows the undulations of the surface. One option is to transform the x-momentum balance equation to the wave-following (χ, ξ)-coordinate system, and to perform the averaging $\langle\rangle_\xi$ keeping ξ rather than z constant. This leads to

$$\left\langle \frac{\partial (h-\eta)\bar{u}}{\partial t} \right\rangle_\xi = \frac{\partial}{\partial \xi}\left(\underbrace{-\langle \overline{u'w'} \rangle_\xi}_{\tau_t/\rho_a} \quad \underbrace{-\langle \bar{u} W \rangle_\xi + \langle \eta_x (\bar{p} + \overline{u'u'})(1-\xi) \rangle_\xi}_{\tau_w/\rho_a} \right), \qquad (5.2)$$

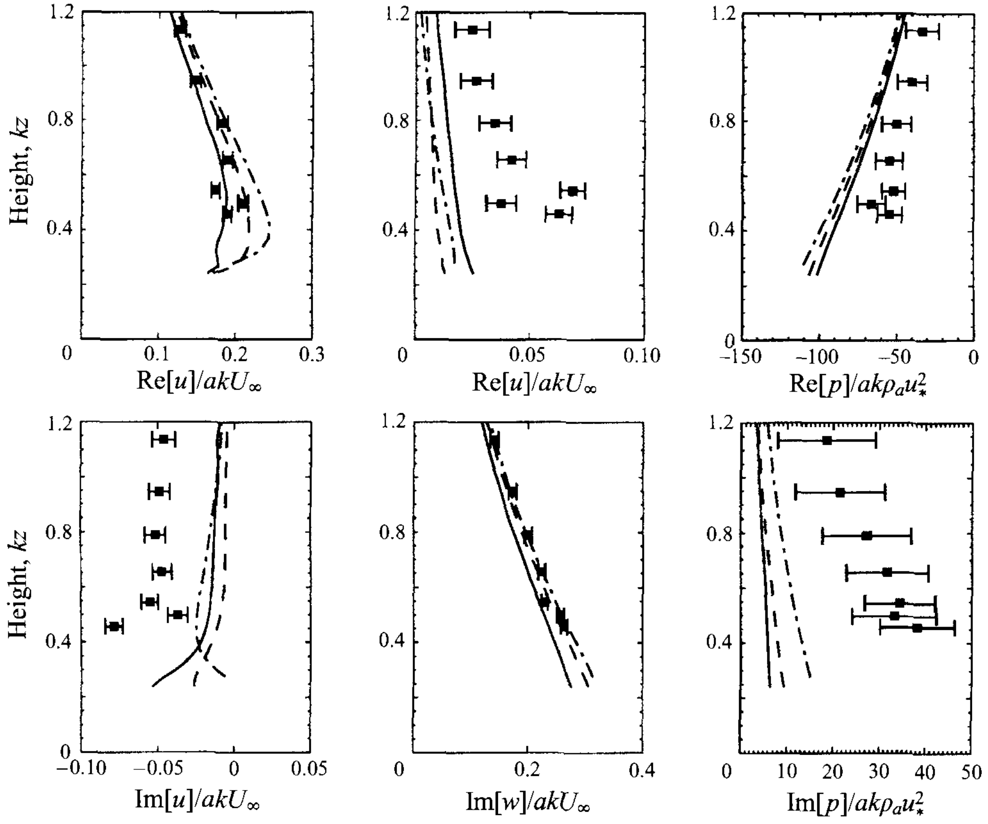

FIGURE 8. Profiles of the wave-induced amplitudes of the horizontal velocity, vertical velocity and pressure for run 35 ($U_\lambda/c = 5.3$). Model results with different turbulence closures are drawn: dash-dotted line, mixing length; dashed line, e-ϵ; solid line, LRR turbulence scheme.

where

$$W = \bar{w} - (1-\xi)(\bar{u}-c)\eta_x. \tag{5.3}$$

Since we assume the flow is stationary, the temporal derivative on the left-hand side of (5.2) is zero. Consequently the sum of the terms between the brackets is independent of height, though each term individually may depend on height. The second and third term between the brackets together represent the wave stress τ_w. The former is zero at the surface $\xi = 0$ owing to the boundary condition $W = 0$ at the surface. Since the latter contribution arises purely because we average over an undulating surface, it will be zero at the top of the domain ξ: when for the averaging at the top ξ is kept constant, the height z is also constant. In other words: when the wave stress through an undulating surface is calculated, correlations between the pressure (and velocity variances) and the slope of this surface will arise.

In figure 11 calculated and observed profiles of the wave stress are shown for run BA. The mixing length closure (dash-dotted line) gives rise to a wave stress that decays exponentially from its surface value to zero with height. The decay is slightly faster than $\exp(-2kz)$, which is shown as a dotted line. In the LRR scheme the wave stress decays from its surface value to zero at the top of the inner region ($kz = 0.09$). At the bottom of the outer region the wave stress shows an overshoot and reverses sign to become negative. Townsend (1972) found a similar behaviour from his numerical

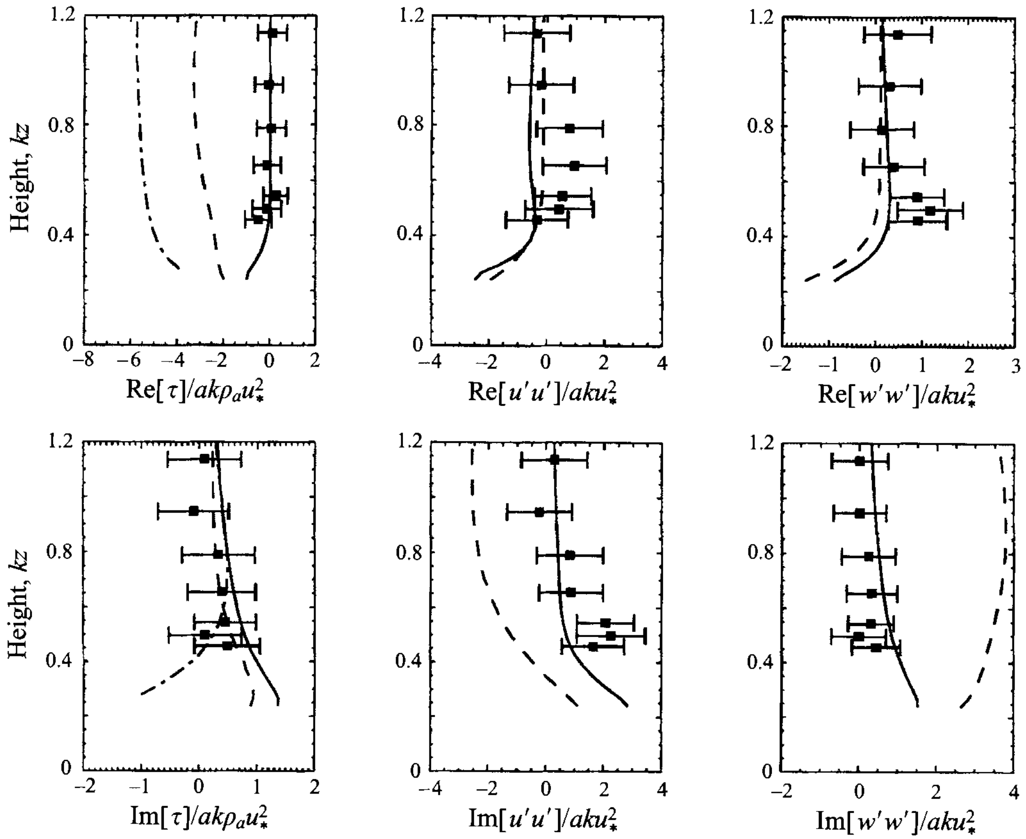

FIGURE 9. Profiles of the wave-induced amplitudes of the stress, and the horizontal and vertical velocity variance for run 35 ($U_\lambda/c = 5.3$). Lines indicate model calculations with different turbulence models (see figure 8).

calculations. The observations of Hsu *et al.* (1981) also show the overshoot (see their figure 14). To enable a comparison with the observed wave stresses, the model results in figure 11 have been normalized to yield the same surface value of the wave stress as the observations. Our observations, also plotted in figure 11, are not close enough to the surface to distinguish between the turbulence parameterizations. This of course is a consequence of the fact that the observations are made at a fixed height, and we have to keep clear of the crests.

6. Discussion

From the observations presented here, it is clear that eddy viscosity closures overestimate wave-induced stresses in the outer region. The LRR model does not show this deficiency. The observations also indicate that the model underestimates the phase shift of the undulating flow in the outer region, and thereby the growth rate of the waves. Two possible causes for this discrepancy are (i) an inadequate description of the (wave-induced) turbulence close to the surface and (ii) a modulation of the aerodynamical surface roughness by wind ripples.

The modelling of turbulence close to a solid wall is notoriously difficult. In the context of a Reynolds stress model, the parameterizations of the pressure-velocity

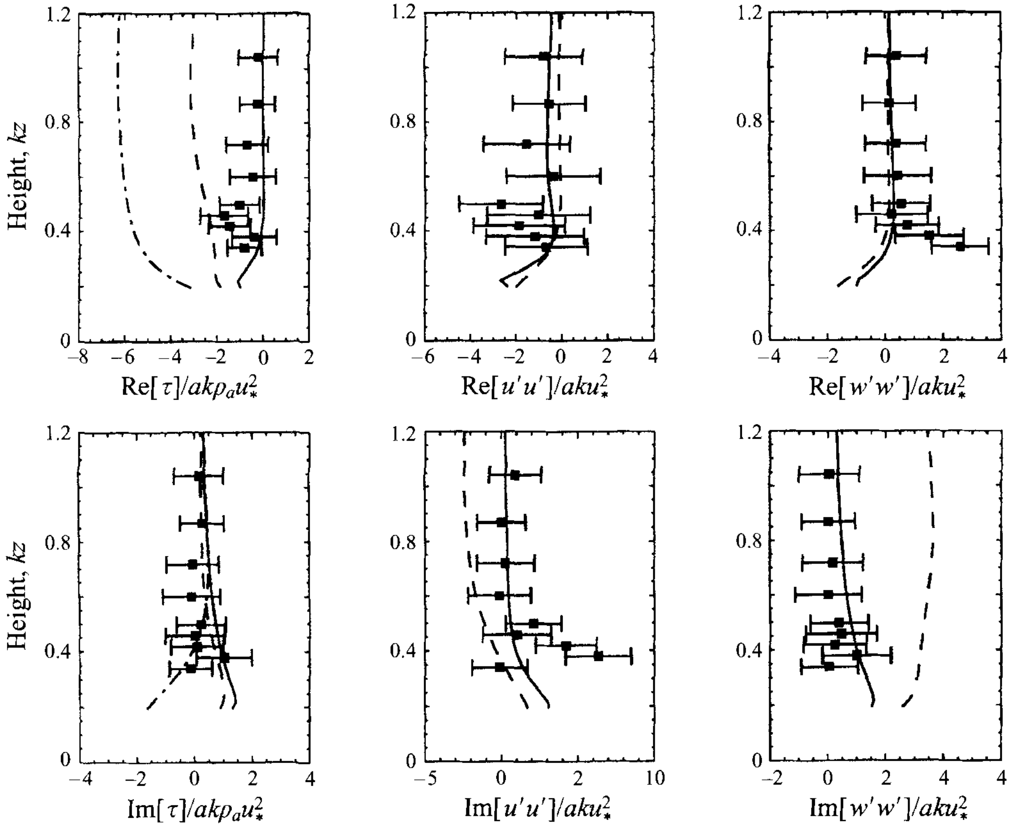

FIGURE 10. As figure 9 for run BA ($U_\lambda/c = 4.6$).

correlation terms $\Pi_{ij}^{(1)}$ and $\Pi_{ij}^{(2)}$ used in the LRR model are not valid close to a solid wall. There are also reasons to believe that the dissipation is not isotropic close to a surface. For small wave Reynolds numbers these wall effects may interfere with the dynamics in the inner region. Harris *et al.* (1996) made calculations with a model that includes low Reynolds number effects. They concluded that these effects become important if the wave Reynolds number, based on wavelength and friction velocity, is lower than 2×10^4. In the present experiment the Reynolds number is of the order of 10^4. Hence the observed increase of the anisotropy of the turbulence towards the surface may be related to low-Reynolds number near-wall effects. These effects are neglected in the LRR model. Several modifications to the parameterization of the pressure–velocity correlation terms and the dissipation term have been proposed, to enable the model to reproduce the well-known distributions of the velocity and velocity variances above a flat plate (e.g. Hanjalić & Launder 1975 and Durbin 1993). However, these methods differ widely and no consensus has been reached on what is the best approach.

An additional complication is that the surface of the paddle wave is not flat, but it is covered by wind ripples. In principle it is possible to resolve the air flow over the individual ripples, and to consider the water surface as a curved but aerodynamically smooth wall. In practice this approach is impossible due to the huge range of scales involved: in the vertical ranging from the top of the ISL of the shortest ripple to the length of the paddle wave. For this reason the effect of the ripples on the

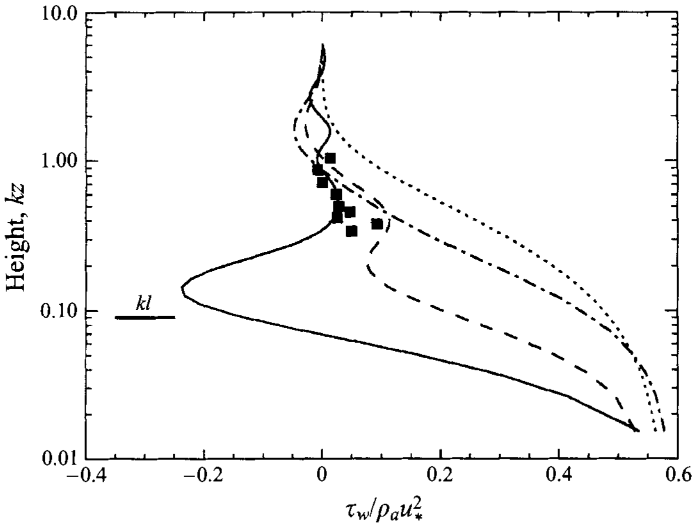

FIGURE 11. The mean wave stress as a function of height kz. According to the mixing length model (dash-dotted line) the wave stress decays slightly faster than $\exp(-2kz)$ (dotted line). In the LRR scheme (solid line) the wave stress decays to zero at the top of the inner region, and shows an overshoot with reversed sign at the bottom of the outer region. The wave stress calculated with the e-ϵ scheme is indicated with the dashed line. The solid squares indicate observed wave stresses in run BA.

roughness of the surface has to be parameterized, as we have done in this study. This means that we no longer consider the surface to be aerodynamically smooth, but transitional or rough depending on the ripples present. These ripples will not be evenly distributed over the phase of the paddle wave, so the roughness will be modulated. Both Gent & Taylor (1976) and Belcher & Hunt (1993) found that a varying roughness could affect the growth rate significantly. We can also use the present model to assess the sensitivity to changes in the roughness. Rather than modulating the surface roughness itself, we will modulate the drag coefficient. This is done to ensure that the variation of the surface roughness itself does not increase the momentum flux. The drag coefficient c_λ is defined as

$$c_\lambda = \frac{\kappa^2}{\ln^2 \lambda/z_0}. \tag{6.1}$$

This drag coefficient is modulated by

$$c_\lambda(x') = \bar{c}_\lambda(1 + ak\hat{c}_\lambda \mathrm{e}^{ikx'}), \tag{6.2}$$

where $x' = x - ct$ and c_λ is the drag coefficient with respect to the height λ. From (6.2) the roughness distribution along the wave can be calculated:

$$z_0(x') = 2\pi e^{-\kappa/(c_\lambda(x'))^{1/2}}. \tag{6.3}$$

In figure 12 the effect on the flow for case 35 is shown. The solid lines represent results from a reference calculation where the roughness distribution is uniform, for the dashed lines a roughness variation with a (real) amplitude of $\hat{c}_\lambda = 4$ was taken. Clearly the imposed roughness variation is capable of shifting the undulating flow downstream, thereby increasing the calculated growth rate from $\beta = 15$ for the constant roughness case, to $\beta = 35$ when $\hat{c}_\lambda = 4$. At present no theory exists

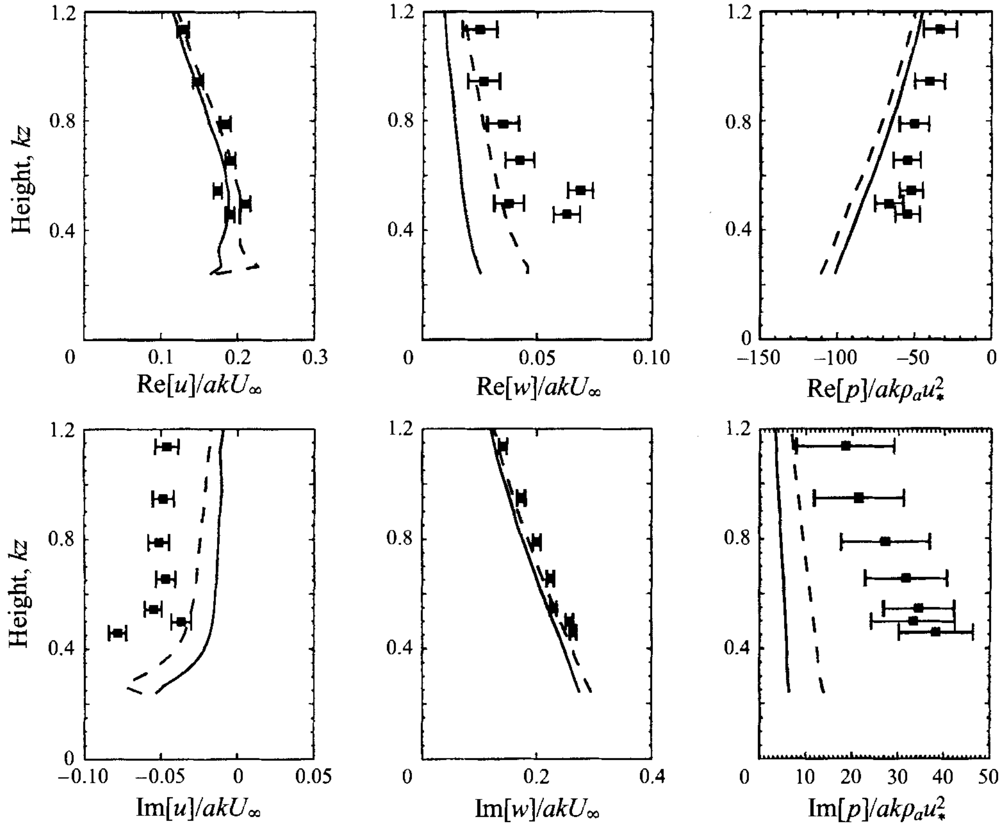

FIGURE 12. Effect of a varying surface roughness on the velocity and pressure perturbations for run 35: solid line, constant roughness ($\hat{c}_\lambda = 0$); dashed line, $\hat{c}_\lambda = 4$.

which allows the calculation of the ripple modulation and the roughness variation it causes.

Though the growth rates calculated with the numerical model underestimate the observed values, it is interesting to compare the growth rates calculated with the different turbulence schemes with some widely used parameterizations. In figure 13 a comparison is made between the growth rates obtained with different theories and the observations of Snyder *et al.* (1981). For the parameterization of the observations of Snyder we use

$$\beta = \frac{1}{4}\left(\frac{c}{u_*}\right)^2 \left(\frac{28u_*}{c} - 1\right), \tag{6.4}$$

which is the form which was used in earlier versions of the WAM wave model (WAMDI 1988). In Snyder *et al.*'s experiment growth rates were observed by measuring the out-of-phase component of the pressure for waves with $1 < U_\lambda/c < 4$.

Using the mixing length closure Jacobs (1987) and van Duin & Janssen (1992) derived analytically

$$\beta = 2.5\kappa \frac{c}{u_*}\left(\frac{U_{1/k}}{c} - 1\right). \tag{6.5}$$

This theory is only valid for slow waves with $U_\lambda/c > 3$. The trend in β as a function of c/u_* agrees with the numerical simulation using the mixing length closure. However,

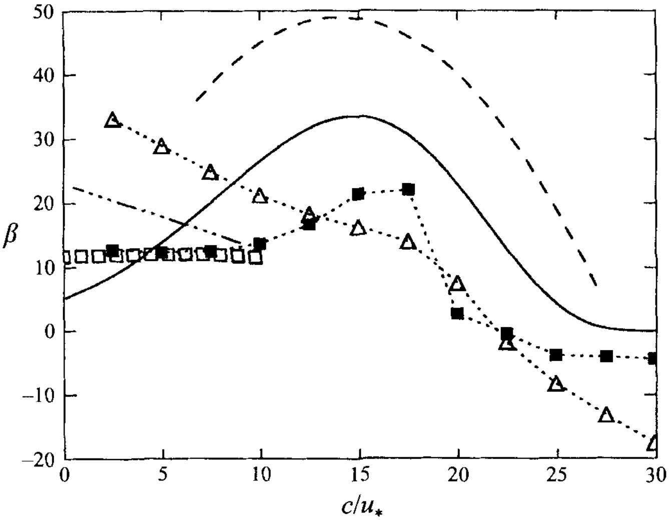

FIGURE 13. The growth rate parameter β *vs.* the ratio c/u_*. The dimensionless roughness kz_0 is 10^{-4}. Full line, growth rate used in WAM Cycle 4 based on Miles (1957); dash-dot-dot-dot, van Duin & Janssen (1992) using mixing length; dashed, parameterization of the Snyder *et al.* (1981) experiment; open squares, Belcher & Hunt (1993). The results from numerical simulations are dotted with: open triangles, mixing length; solid squares, LRR model.

compared to the numerical model van Duin & Janssen underestimate the growth rate by 30%. According to Jenkins (1992) this is due to a slow convergence of the asymptotic expansions used by Jacobs (1987) and van Duin & Janssen (1992). He claims kz_0 has to be as small as 10^{-8} for (6.5) to be within 10% of the growth rate following from mixing length closure. Wood & Mason (1993) argue that the stress variations in the inner region are treated inadequately by Jacobs and van Duin & Janssen.

The growth rate used in the most recent version of the WAM model (Cycle 4) is based on a parameterization of the theory of Miles (1957) proposed by Janssen (1991):

$$\beta = \frac{1.2}{\kappa^2}\mu \ln^4 \mu, \tag{6.6}$$

where μ is the dimensionless critical height:

$$\mu = \min\left[1, kz_0 \exp\left(\frac{\kappa}{u_*/c + \alpha}\right)\right]. \tag{6.7}$$

Relative to the parameterization of the growth rate obtained with Miles' theory ($\alpha = 0$ in the above equation), the growth rate used in the WAM model ($\alpha = 0.011$) results in a considerably larger energy input to the waves with a phase speed comparable to the wind speed. Note that Miles' theory does not yield negative growth rates for waves faster than the wind (no critical height) and that the growth of very short waves quenches as the critical height goes to zero.

Also plotted in figure 13 are the growth rates obtained with the analytical theory of Belcher & Hunt (1993), kindly provided by the first author. This theory is only valid for slow waves with $c/u_* < 10$ and if the inner region is thin enough, which imposes the condition $kz_0 < 10^{-3}$. The contribution from the shear stress modulation at the surface, responsible for a significant part of the energy flux according to the article of Belcher & Hunt (1993), is discarded here. As was the case for the sheltering coefficients of hills (see figure 3) the theory of Belcher & Hunt is in excellent agreement with the LRR model.

7. Conclusions

The comparison of laboratory observations over water waves with numerical simulations shows that turbulence closure schemes based on the eddy viscosity concept overestimate the modulation of the turbulent shear stress in the outer region. A similar overestimation was found by Belcher *et al.* (1993) in stress profiles observed over hills. Eddy viscosity schemes imply that the turbulent eddies are in equilibrium with the instantaneous shear at each point in the flow. Physical scaling arguments explain that this assumption is violated in the outer region of the flow over waves. Numerical simulations with the LRR model, which does not rely on an eddy viscosity, show good agreement with the observations of the shear stress modulation in the outer region.

When eddy viscosity closure schemes are used to parameterize turbulence in the flow over waves, an additional growth mechanism is introduced that dominates other mechanisms (Belcher *et al.* 1993). Elimination of this erroneous contribution gives rise to a different dependence of the growth rate on external parameters like the ratio c/u_* and the surface roughness. Both the growth rate for slow waves ($U_\lambda/c > 2$) and the decay rate for fast waves ($U_\lambda/c < 1.2$) are significantly reduced on going from a mixing length closure to a Reynolds stress model, whereas the growth rate for waves travelling almost as fast as the wind is increased. The growth rates calculated with the Reynolds stress model are in excellent agreement with results from the analytical model presented in Belcher & Hunt (1993).

Three different ratios of the wind speed and phase speed of the paddle wave are used in the experiment: $U_\lambda/c = 2.8$, 4.6 and 5.3. The observed amplitude of both the pressure and the velocity perturbations shows excellent agreement with the simulations. This is a strong indication that our new experimental procedure, i.e. turning off the wave maker before starting the data acquisition to eliminate its spurious effect on the pressure observations, does not affect the actual flow of the air over the waves. Comparison of the observed phase of the pressure and velocity perturbations for the last two cases with numerical simulations reveals that the model underpredicts the downwind phase shift of the undulating flow by approximately a factor 4. Since this downwind shift induces the out-of-phase pressure on the surface of the wave which makes the wave grow, the numerical model underestimates the observed growth rate. In the first set of observations, with the lowest wind speed/phase speed ratio, the large scatter prevents detailed conclusions. Among the possible explanations of the underestimation of the growth rate for slow waves are an inadequate parameterization of the turbulence in the inner region and a roughness modulation of the paddle wave surface by wind ripples. It is suggested that the dissipation and pressure-correlation terms in the Reynolds stress be modified analogously to suggestions made for flow over flat plates. The role of the roughness modulation by ripples also needs further investigation.

The authors would like to thank Stephen Belcher for providing form drags and growth rates following from the theory presented in Belcher & Hunt (1993). C. Mastenbroek was supported by the Netherlands Geosciences Foundation (GOA) with financial aid from the Netherlands Organisation for Scientific Research (NWO).

In France this work was supported by PATOM/DRET Program (grant 93 2537 A) and by the Office of Naval Research (grant N00014-93-1-0500).

Appendix. Description of the second-order LRR model

The functional dependence of the production term follows from the basic equations and needs no parameterization:

$$P_{ij} = -\overline{u_i'u_k'}\frac{\partial \bar{u}_j}{\partial x_k} - \overline{u_j'u_k'}\frac{\partial \bar{u}_i}{\partial x_k} \tag{A 1}$$

(note that $P = \frac{1}{2}P_{ii}$). The turbulent transport of the Reynolds stresses is parameterized as

$$T_{ij} = c_s\frac{\partial}{\partial x_k}\left\{\frac{e}{\epsilon}\left(\overline{u_i'u_m'}\frac{\partial \overline{u_j'u_k'}}{\partial x_m} + \overline{u_j'u_m'}\frac{\partial \overline{u_i'u_k'}}{\partial x_m} + \overline{u_k'u_m'}\frac{\partial \overline{u_i'u_j'}}{\partial x_m}\right)\right\}. \tag{A 2}$$

The pressure–velocity correlation terms are thought to relax the stresses towards isotropy, and to reduce the effectiveness of the production. For the first part of the pressure–velocity correlation term, $\Pi_{ij}^{(1)}$, the Rotta hypothesis is used:

$$\Pi_{ij}^{(1)} = -2c_1\epsilon b_{ij}, \tag{A 3}$$

where b_{ij} is the stress-anisotropy tensor defined as

$$b_{ij} = \frac{\overline{u_i'u_j'}}{2e} - \tfrac{1}{3}\delta_{ij}. \tag{A 4}$$

The second part of Π_{ij} is called the rapid term, and it is parameterized as:

$$\Pi_{ij}^{(2)} = 4e\left\{\tfrac{1}{5}S_{ij} + \frac{9c_2+6}{22}\left(S_{ik}b_{kj} + S_{kj}b_{ik} - \tfrac{2}{3}S_{kl}b_{kl}\delta_{ij}\right) + \frac{10-7c_2}{22}(R_{ik}b_{kj} + R_{kj}b_{ik})\right\}, \tag{A 5}$$

where R_{ij} is the mean vorticity tensor:

$$R_{ij} = \frac{1}{2}\left(\frac{\partial \bar{u}_i}{\partial x_j} - \frac{\partial \bar{u}_j}{\partial x_i}\right). \tag{A 6}$$

The dissipation is given by

$$\epsilon_{ij} = \tfrac{2}{3}\delta_{ij}\epsilon. \tag{A 7}$$

The isotropic dissipation rate ϵ is calculated with the same dynamical equation as in the e-ϵ scheme, i.e. equation (3.10). The only difference is the parameterization of the turbulent transport term: in order to eliminate the eddy viscosity completely from the second-order model, equation (3.13) is replaced by

$$\overline{\epsilon' u_i'} = -c_\epsilon\frac{e}{\epsilon}\overline{u_i'u_k'}\frac{\partial \epsilon}{\partial x_k}. \tag{A 8}$$

The LRR scheme needs six constants. Again we use the standard values for these parameters in this study (Launder *et al.* 1975): $c_{1\epsilon}$ =1.44, $c_{2\epsilon} = 1.92$, $c_s = 0.11$, $c_1 = 1.5$, $c_2 = 0.4$ and $c_\epsilon = 0.267$.

REFERENCES

AL-ZANAIDI, M. A. & W. H. HUI, 1984 Turbulent airflow over water waves – a numerical study. *J. Fluid Mech.* **148**, 225–246.

Banner, M. L. 1990 The influence of wave breaking on the surface distribution in wind-wave interactions *J. Fluid Mech.* **211**, 463–495.

Batchelor, G. K. & Proudman, L. 1954 The effect of rapid distortion on a fluid in a turbulent motion. *Q. J. Mech. Appl. Math.* **7**, 83–103.

Belcher, S. E., Harris, J. A. & Street, R. L. 1994 Linear dynamics of wind waves in coupled turbulent air-water flow. Part 1. Theory. *J. Fluid Mech.* **271**, 119–151.

Belcher, S. E. & Hunt, J. C. R. 1993 Turbulent shear flow over slowly moving waves. *J. Fluid Mech.* **251**, 109–148.

Belcher, S. E., Newley, T. M. J. & Hunt, J. C. R. 1993 The drag on an undulating surface induced by the flow of a turbulent boundary layer. *J. Fluid Mech.* **249**, 557–596.

Britter, R.E., Hunt, J. C. R. & Richards, K. J. 1981 Air flow over a two-dimensional hill: studies of velocity speed-up, roughness effects and turbulence. *Q. J. R. Met. Soc.* **107**, 91–110.

Burgers, G. & Makin, V. K. 1993 Boundary-layer model results for wind-sea growth. *J. Phys. Oceanogr.* **23**, 372–385.

Chalikov, D. V. 1978 The numerical simulation of wind-wave interaction. *J. Fluid Mech.* **87**, 561–582.

Donelan, M. A. 1987 The effect of swell on the growth of wind waves. *Johns Hopkins APL Technical Digest* **8**, 18–23.

Duin, C. A. van & Janssen, P. A. E. M. 1992 An analytic model of the generation of surface gravity waves by turbulent air flow. *J. Fluid Mech.* **236**, 197–215.

Durbin, P. A. 1993 A Reynolds stress model for near-wall turbulence. *J. Fluid Mech.* **249**, 465–498.

Favre, A. & Coantic, M. 1974 Activities in, and preliminary results of, air-sea interactions research at IMST. *Adv. Geophys.* **18A**, 391–405.

Gent, P. R. & Taylor, P. A. 1976 A numerical model of the air-flow over waves. *J. Fluid Mech.* **77**, 105–128.

Giovanangeli, J. P. 1980 A non dimensional heat transfer law for a slanted hot-film in water flow. *DISA Information No* 25.

Giovanangeli, J. P. 1988 A new method for measuring static pressure fluctuations with application to wind wave interaction. *Exps. Fluids* **6**, 156–164.

Giovanangeli, J. P. & Chambaud, P. 1987 Pressure, velocity and temperature sensitivities of a bleed-type pressure sensor. *Rev. Sci. Instrum.* **58**, 1221–1225.

Hanjalić, K. & Launder, B. E. 1975 Contribution towards a Reynolds-stress closure for low-Reynolds-number turbulence. *J. Fluid Mech.* **74**, 593–610.

Harris, J. A., Belcher, S. E. & Street, R. L. 1996 Linear dynamics of wind waves in coupled turbulent air-water flow. Part 2. Numerical model. *J. Fluid Mech.* **308**, 219–254.

Hsu, C. T. & Hsu, Y. 1983 On the structure of turbulent flow over a progressive water wave: theory and experiment in a transformed, wave-following coordinate system. Part 2. *J. Fluid Mech.* **131**, 123–153.

Hsu, C. T., Hsu, Y. & Street, R. L. 1981 On the structure of turbulent flow over a progressive water wave: theory and experiment in a transformed, wave-following coordinate system. *J. Fluid Mech.* **105**, 87–117.

Hunt, J. C. R., Leibovich, S. & Richards, K. J. 1988 Turbulent shear flows over low hills. *Q. J. R. Met. Soc.* **114**, 1435–1471.

Jackson, P. S. & Hunt, J. C. R. 1975 Turbulent wind flow over a low hill. *Q. J. R. Met. Soc.* **101**, 929–955.

Jacobs, S. J. 1987 An asymptotic theory for the turbulent flow over a progressive water wave. *J. Fluid Mech.* **174**, 69–80.

Janssen, P. A. E. M. 1991 Quasi-linear theory of wind wave generation applied to wave forecasting. *J. Phys. Oceanogr.* **21**, 1631–1642.

Jenkins, A. D. 1992 A quasi-linear eddy-viscosity model for the flux of energy and momentum to wind waves using conservation-law equations in a curvilinear coordinate system. *J. Phys. Oceanogr.* **22**, 843–858.

Jones, W. P. & Launder, B.E. 1972 The predictions of laminarisation with a two equation model of turbulence. *Intl J. Heat Mass Transfer* **15**, 301.

Latif, M. A. 1974 Acoustic effects on pressure measurements over water waves in the laboratory. *Tech. Rep.* 25. Coastal and Oceanographic Engineering Laboratory Gainesville, Florida.

Launder, B. E., Reece, G. J. & Rodi, W. 1975 Progress in the development of a Reynolds-stress turbulence closure. *J. Fluid Mech.* **68**, 537–566.

MAKIN, V. K. 1979 The wind field above waves. *Oceanology* **19**, 127–130.

MILES, J. W. 1957 On the generation of surface waves by shear flows. *J. Fluid Mech.* **3**, 185–204.

PAPADIMETRAKIS, Y. A., HSU, Y. & STREET, R. L. 1986 The role of wave-induced pressure fluctuations in the transfer across an air-water interface. *J. Fluid Mech.* **170**, 113–137.

PLANT, W. J. 1982 A relation between wind stress and wave slope. *J. Geophys. Res.* **87**(C), 1961–1967.

RESCH, F. 1973 Use of dual sensor hot-film probe in water flow. *DISA Information No* 14.

SHIH, T. H. & LUMLEY, J. L. 1993 Critical comparison of second-order closures with direct numerical simulation of homogeneous turbulence. *AIAA J.* **31**, 663–670.

SNYDER, R. L., DOBSON, F. W. ELLIOTT, J. A. & LONG, R. B. 1981 Array measurements of atmospheric pressure fluctuations above surface gravity waves. *J. Fluid Mech.* **102**, 1–59.

STEWART, R. H. 1970 Laboratory studies of the velocity field over deep-water waves. *J. Fluid Mech.* **42**, 733–754.

TOWNSEND, A. A. 1972 Flow in a deep turbulent boundary layer over a surface distorted by water waves. *J. Fluid Mech.* **55**, 719–735.

TOWNSEND, A. A. 1980 The response of sheared turbulence to additional distortion. *J. Fluid Mech.* **81**, 171–191.

WAMDI GROUP 1988 The WAM model - A third-generation ocean wave prediction model. *J. Phys. Oceanogr.* **18**, 1775–1810.

WOOD, N. & MASON, P. 1993 The pressure force induced by neutral, turbulent flow over hills. *Q. J. R. Met. Soc.* **119**, 1233–1267.

ZEMAN, O. & JENSEN, N. O. 1987 Modification of turbulence characteristics in flow over hills. *Q. J. R. Met. Soc.* **113**, 55–80.